Multi-site synergistic hydrogen evolution reactions on porous homogeneous FeCoNiCu high-entropy alloys fabricated by solution combustion synthesis and hydrogen reduction

Fei Guo [a,b,1], Yilin Zhang [a,1], Botao Shen [c,1], Leilei Wan [a], Guangya Hou [a], Huazhen Cao [a], Guoqu Zheng [a], Yonghao Zhao [b,d,*], Huibin Zhang [a,**]

[a] College of Materials Science and Engineering, Zhejiang University of Technology, Hangzhou 310014, China
[b] Nano and Heterogeneous Materials Center, School of Materials Science and Engineering, Nanjing University of Science and Technology, Nanjing 210094, China
[c] Advanced Materials Division, Suzhou Institute of Nano-Tech and Nano-Bionics, Chinese Academy of Sciences, Suzhou 215123, China
[d] School of Materials Science and Engineering, Hohai University, Changzhou 213200, China

A B S T R A C T

A combination process of solution combustion synthesis and hydrogen reduction was proposed to prepare porous homogeneous FeCoNiCu high-entropy alloys (HEAs) for hydrogen evolution reaction (HER). Solution combustion synthesis was herein employed to obtain the multiple composite oxide precursor with tunable molar ratio of elements and pore structure, as well as uniform element distribution. The generated bulk porous HEAs composed of single-phase solid solution were achieved by hydrogen reduction of the oxide precursor at optimal temperature. The porous structure and specific surface area of oxide precursor and reduced HEA could be adjusted by varying the mass ratio of metal nitrates to glycine and the reduction temperature. The prepared $FeCoNiCu_{0.5}$ HEA with enriched porosity and high specific surface area showed high catalytic activity and excellent electrochemical stability during alkaline HER. Density functional theory (DFT) calculation revealed the electronic interaction between Fe, Co, Ni and Cu elements facilitated the efficiency for H* adsorption and H_2 desorption, and enhanced the catalytic activity of the Co/Ni sites. This work provided an approach to develop porous high-entropy alloy catalysts for HER and other applications.

1. Introduction

Nowadays the development of clean energy has become extremely urgent in face of increasingly severe environmental pollution and energy depletion issues[1–3]. Hydrogen, as a low-cost, high-energy density, and pollution-free clean energy, has the potential to replace traditional fossil fuels[4–7]. Electrolysis of water is widely regarded as an effective strategy for hydrogen production. Especially, the electrolytic method of hydrogen production can convert the intermittent renewable energy power into high-quality green hydrogen product, which has become a key focus of research and industrialization[8–14]. However, investment and operating costs remain the "roadblock" to large-scale commercialization of this technology, especially the significant use of expensive noble metal electrocatalysts. In order to address this problem, researchers have turned their attention to low-cost transition metals such as Co, Fe, Ni, Mn, Cu, etc., as well as their related alloys and compounds, which show activities comparable to those achieved with Pt catalysts [10,15–18].

In recent years high-entropy alloys (HEAs), composed of three or four metal elements, have become a type of newly-emerging electrocatalysts for various applications including hydrogen production [19–23]. Due to the synergistic effect among the various components, HEAs exhibit extremely efficient electron transfer characteristics and excellent catalytic activity, even when composed solely of low-cost non-precious transition metal elements[24–28]. He et al. reported that the synthesized face-centered cubic FeCoNiWMo HEA catalyst exhibited

Fig. 1. Schematic diagram of the preparation process of porous FeCoNiCu$_x$ HEAs.

an overpotential of only 35 mV at a current density of 10 mA·cm^{-2} under alkaline conditions[29]. The atoms in this HEA could selectively occupy lattice sites, making the protons easier to traverse the energy barrier. Liu et al. prepared a dendritic FeCoNiAlTi high-entropy intermetallic (HEI) catalyst using a method involving melt spinning and dealloying[30]. The unique L1$_2$-type ordered structure of HEI provides a specific site isolation effect, stabilizing the adsorption and dissociation of H$_2$O/H*. This HEI exhibits an overpotential of only 88.2 mV at 10 mA·cm^{-2} with a Tafel slope of only 40.1 mV·dec^{-1} under alkaline conditions. Kasatikov et al. revealed that the lone pair electrons on Ni 3d and the empty orbitals are far from the Fermi level in AlCrCuFeNi HEA, while the empty orbitals on Cr 3d move towards the Fermi level[31]. This phenomenon enhances the electron transfer capability of HEA, thereby boosting the material's catalytic activity. In summary, it is well-acknowledged that the synergistic effect among the elements in HEAs enhances the electrocatalytic activity of common transition metals.

Although HEAs hold broad prospects for functional applications such as catalysis, the catalytic performance is actually influenced by the material morphology and size. In recent years, methods such as carbothermal shock synthesis, liquid-phase synthesis, and laser ablation synthesis have been developed to prepare nano-sized HEAs[21,32–35]. However, the low-dimensional nano-sized HEAs are usually required to be loaded on catalyst support, which limits electronic contact efficiency and service life[36]. Actually, the anti-corrosive conductive HEAs with inherent catalytic activity make them suitable for being developed into structurally functional integrated catalytic electrodes. In general, the scalable commercial catalysts are usually endowed with porous structure which not only provides abundant catalytic active sites due to the high surface area, but also enables the efficient electrolyte diffusion and rapid gas bubble escape[37–41].

Moreover, it is believed that the homogeneous distribution of various elements in HEAs favors the corrosion resistance and the consistency of catalytic sites[20], but immiscible elements such as Cu are liable to form phase-separated heterogeneous structures[42–44]. Solution combustion method is commonly used for the preparation of metal oxide powders [45,46], and is characterized of energy efficiency, low cost, and rapid synthesis. With the aid of solution combustion method, uniformly distributed oxide precursor with porous structure can be obtained. Combined with the hydrogen reduction process, it is possible to obtain porous homogeneous high-entropy alloys. In this study, porous FeCoNiCu HEA are prepared through glycine-metal nitrate combustion

synthesis and low-temperature hydrogen reduction. The effects of process parameters of glycine combustion and hydrogen reduction on the properties of the synthesized porous FeCoNiCu HEA materials are investigated. The electrochemical hydrogen evolution performance of porous FeCoNiCu HEA materials is studied, and the synergistic effect of various elements in enhancing catalytic performance is theoretically unraveled by density functional theory (DFT) calculations.

2. Experimental

2.1. Materials

Iron nitrate nonahydrate (Fe(NO$_3$)$_3$·9 H$_2$O) and copper nitrate trihydrate (Cu(NO$_3$)$_2$·3 H$_2$O) were purchased from China National Pharmaceutical Group Co., Ltd (China). Cobalt nitrate hexahydrate (Co (NO$_3$)$_2$·6 H$_2$O), Nickel nitrate hexahydrate (Ni(NO$_3$)$_2$·6 H$_2$O) and Glycine (C$_2$H$_5$NO$_2$) were purchased from Shanghai Maclean Biochemical Technology Co., Ltd. (China). All the reagents were analytically pure.

2.2. Preparation of porous FeCoNiCu HEA

Porous FeCoNiCu HEA were synthesized via glycine-triggered self-propagating combustion followed by hydrogen reduction. Firstly, the preparation of FeCoNiCu$_x$ HEAs, where Fe, Co, Ni were in equimolar ratio and the molar ratio of Cu was 0, 0.5, and 1.0, respectively, were started with Fe(NO$_3$)$_3$·9 H$_2$O, Co(NO$_3$)$_2$·6 H$_2$O, Ni(NO$_3$)$_2$·6 H$_2$O, and Cu (NO$_3$)$_2$·3 H$_2$O. The mass ratio of nitrates to glycine (C$_2$H$_5$NO$_2$) was adjusted in the range of 6:1, 8:1 and 10:1. The mixed nitrates and glycine were dissolved in distilled water with continuous stirring. The solution was then heated and evaporated to concentrate, during which glycine and metal ions underwent chelation reactions and sol-gel transition took place.

Further heating and evaporation would trigger the combustion of glycine, and the released gas can transform the gel into fluffy composite precursor oxides. After that, the precursor oxide powder was loaded loosely in a sintering boat, which was then placed in a tube furnace for hydrogen reduction. The reduction temperature was 300–700 °C and the reduction time was 2 hours. After cooling in the furnace, the porous FeCoNiCu$_x$ HEAs were obtained. The schematic diagram of the preparation process is shown in Fig. 1, and the relevant experimental details
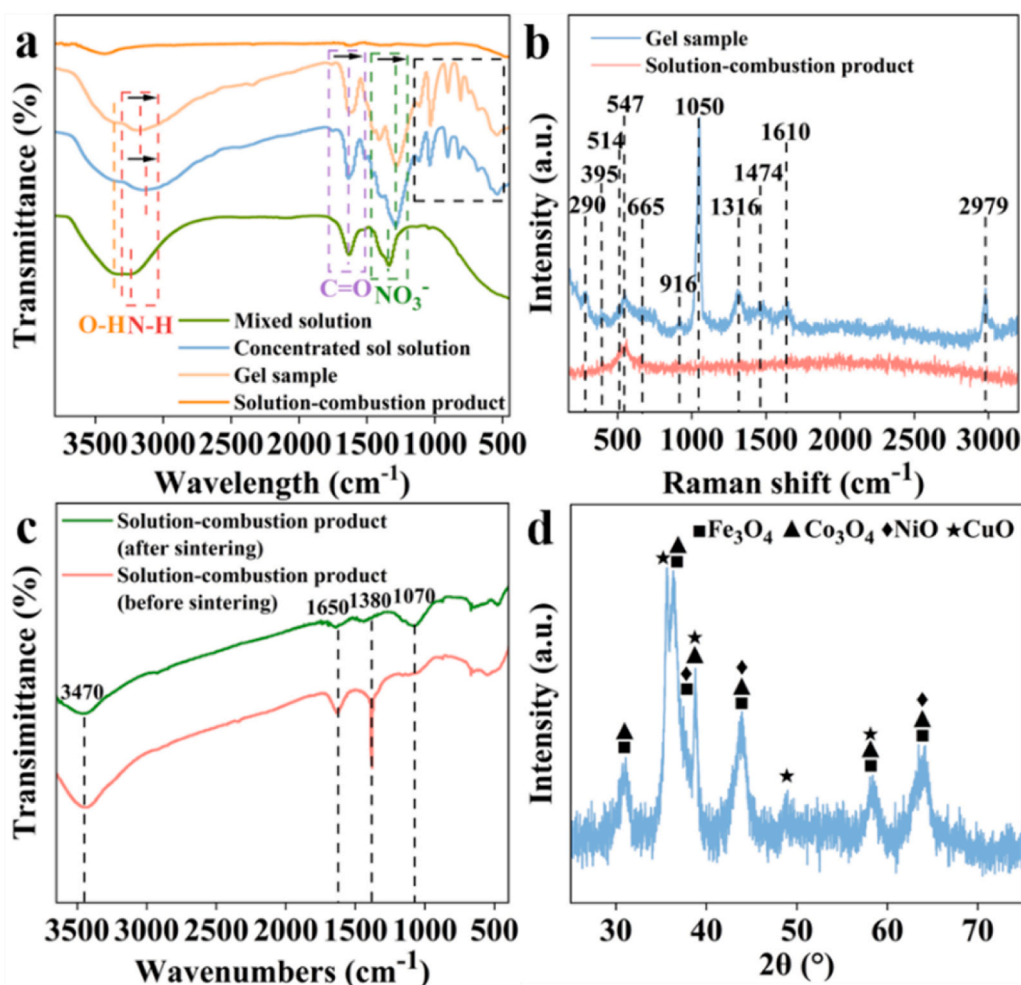
Fig. 2. (a) Infrared spectra of the mixed solution, concentrated sol solution, gel sample, and solution-combustion product. (b) Raman spectra of gel sample, and solution-combustion product. (c) Infrared spectra of solution-combustion product before and after calcination. (d) XRD patterns of composite oxide precursors.

are illustrated in Fig. S1.

2.3. Electrochemical measurements

Electrochemical measurements were conducted on a CHI660E electrochemical workstation (Shanghai Chenhua Instrument Corporation, China). To prepare the catalyst-coated working electrode, the as-synthesized catalyst (5 mg) was dispersed in the solution of water/ethanol/Nafion solution (5.0 wt%) (500 μL/460 μL/40 μL) under sonication for 1 h to form a homogeneous catalyst ink. Then the catalyst rotating ink (15 μL) was loaded onto glassy carbon electrodes (diameter 3 mm) in sequence and dried in air. A Hg/HgO electrode was used as the reference electrode, and a platinum foil was used as the counter electrode. All recorded potentials were converted to reversible hydrogen electrode (RHE). Linear sweep voltammetry (LSV) of the samples was measured in 1 M KOH solution at a scan rate of 10 mV·s^{-1}. The measurements range was selected as ±0.05 V vs. RHE. Cyclic voltammetry (CV) curves of the samples were measured at scan rates of 10, 25, 50, 100, and 150 mV·s^{-1}, with the difference in current density between the anodic and cathodic scans at open circuit potential as the vertical axis to determine the double-layer capacitance. The ECSA of each sample was obtained by applying the corresponding treatment to C$_{dl}$ using the specific formula[13]:

$$ECSA = \frac{C_{dl}}{C_s} \qquad (1)$$

The C$_{dl}$ is the double-layer capacitance, and the C$_s$ is the specific capacitance of the testing solution, typically 0.04 mF·cm^{-2} for 1 M KOH. Electrochemical impedance spectroscopy was performed in the frequency range of 100 kHz to 100 mHz, with the initial potential set to the open circuit potential of the electrode. After 1000 cycles of cyclic voltammetry at a scan rate of 10 mV·s^{-1}, linear sweep voltammetry was measured again. The CA curves were carried out at the corresponding potential to evaluate the HER stability. The water electrolysis (OER// HER) performances were conducted in 1.0 M KOH using the porous FeCoNiCu$_x$ HEAs as both the anode and cathode in a two-electrode system. The polarization curves were recorded with a scan rate of 5 mV·s^{-1}. TOF reveals the reaction rate on a single active site and expresses the intrinsic activity of the catalyst. The specific formula for TOF is[13]:

$$TOF = \frac{jA}{znF} \qquad (2)$$

where j is the current density at a given overpotential; A is the working area; z is the number of electrons involved in the reaction; n is the amount of active material per active site, and F is the Faraday constant.

2.4. Material characterizations

X-ray diffraction (XRD, RIGAKU D/Max 2550 PC, Cu Kα, 40 kV, 40 mA, scanning rate 20° min^{-1}) was used to investigate the phase composition of the samples. Infrared spectroscopy (Thermo Nicolet
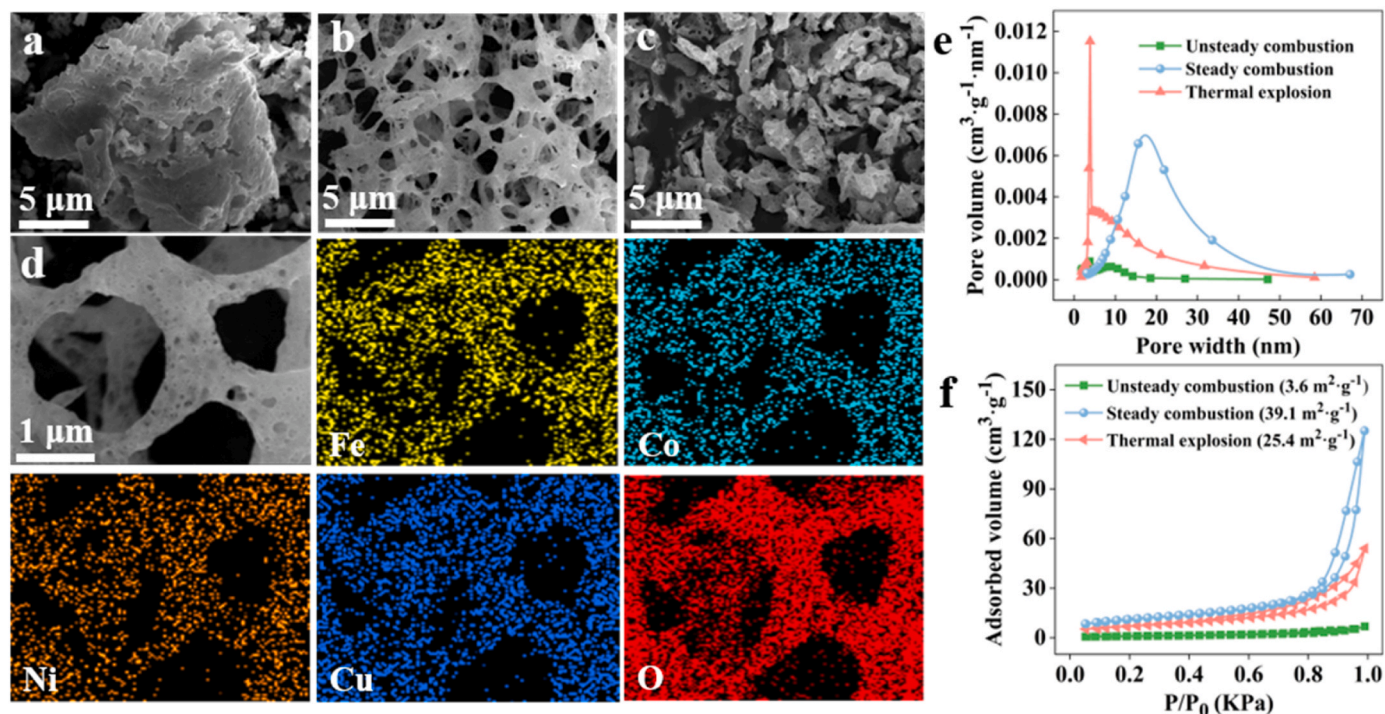
Fig. 3. (a) SEM images of the FeCoNiCu$_{0.5}$ precursor salt and the corresponding EDS surface scanning images. (b)-(d) Morphology of the precursors synthesized with a mass ratio of metal nitrates to glycine of 10:1 (unsteady combustion), 8:1 (steady combustion), and 6:1 (thermal explosion). (e) Pore size distribution and (f) adsorption-desorption curve of the precursors under the three combustion states.

Nicolet 670) and Raman spectra (Thermo Scientific DXR2) were employed to record the structural changes of the products at different stages during the preparation process. The morphology of the material was observed using a scanning electron microscope (SEM, SUPRA 55, Zeiss Merlin, operated at 20 kV) equipped with an energy-dispersive spectrometer (EDS, GENENIS-4000, PHILIPS). Transmission electron microscopy (TEM, TECNAI G2 F30 S-TWIN) images and elemental distribution spectrometer (EDS) mapping were captured at 300 kV. The specific surface area, average pore size, and adsorption-desorption isotherms were analyzed using the Brunauer-Emmett-Teller (BET, 3 H-2000PS1) method. X-ray photoelectron spectroscopy (XPS, Kratos AXIS Ultra DLD) was used to study the surface chemical state and composition of the samples, and the binding energy was calibrated based on C 1 s=284.6 eV.

2.5. Density functional theory (DFT) calculation

To understand the impact of the synergistic effect toward HER, theoretical calculations were performed using density functional theory (DFT) implemented in the Vienna Ab initio Simulation Package (VASP). The exchange-correlation potential was described by using the generalized gradient approximation of Perdew-Burke-Ernzerhof (GGA-PBE). The projector augmented-wave (PAW) method was employed to treat interactions between ion cores and valence electrons. The plane-wave cutoff energy was fixed to 500 eV. Given structural models were relaxed until the Hellmann–Feynman forces smaller than −0.02 eV·Å^{-1} and the change in energy smaller than 10^{-5} eV was attained. The Brillouinzone integration sampling was using 6×6×1 k-points meshes for the surface slabs. Based on the XRD and HR-TEM results, the Co$_{0.039}$Cu$_{0.003}$Fe$_{0.262}$Ni$_{0.695}$ (111) slab model is adopted to model the FeCoNiCu$_{0.5}$ surface. The molar ratio of Fe: Co: Ni: Cu was set at 1:1:1:0.5. Grimme's DFT-D3 methodology was used to describe the dispersion interactions among all the atoms in adsorption models. In free energies calculations, the entropic corrections and zero-point energy (ZPE) have been included. The free energy of species was calculated

according to the standard formula:

$$\Delta G = E + \Delta ZPE + \Delta H - \Delta TS \tag{3}$$

where ZPE was the zero-point energy, ΔH was the integrated heat capacity, T was the temperature of product, and S was the entropy.

3. Results and discussion

3.1. Synthesis and characterization of porous FeCoNiCu$_x$ HEAs

The gelation transition and the rapid self-propagating combustion dehydration during the combustion synthesis process play a crucial role in obtaining the uniformly mixed oxide precursor. In order to reveal the reaction mechanism of this process, spectroscopic methods were employed to analyze the intermediate products (Fig. 2). The FTIR spectra of the mixed solution shown in Fig. 2(a) display the absorption peak of hydroxyl (-OH) near 3470 cm^{-1}[47], the amino (-N-H) absorption peak near 3200 cm^{-1}[48], the carbonyl (-C=O) absorption peak near 1650 cm^{-1}[48], and the characteristic absorption peaks of nitrate (-NO$_3$) near 1380 cm^{-1}[49]. While as for the concentrated sol solution and gel sample, the above function groups exhibit a shift to the right, indicating changes in the chemical bond lengths and the formation of new chemical coordination between the function groups. In particular, many new absorption peaks appear in the fingerprint area of the concentrated sol solution and gel sample, which may be attributed to the metal-oxygen (M-OH) coordination bonds. After combustion reactions, the main above absorption peaks disappear, indicating the destruction of organic functional groups and bound water take place. The Raman spectra in Fig. 2(b) confirms this transition. It is seen that in the Raman spectrum of gel sample there are several covalent metal-oxygen bonds below 700 cm^{-1}, including the Cu-O peaks near 290 cm^{-1} and 395 cm^{-1}[50], the Ni-O Raman peak near 514 cm^{-1} [50], the Fe-O Raman peak near 547 cm^{-1}[51], and the Co-O peak near 665 cm^{-1}[52]. In addition, the characteristic absorption peaks including the stretching peak of -C-C near 916 cm^{-1}, the vibration peak
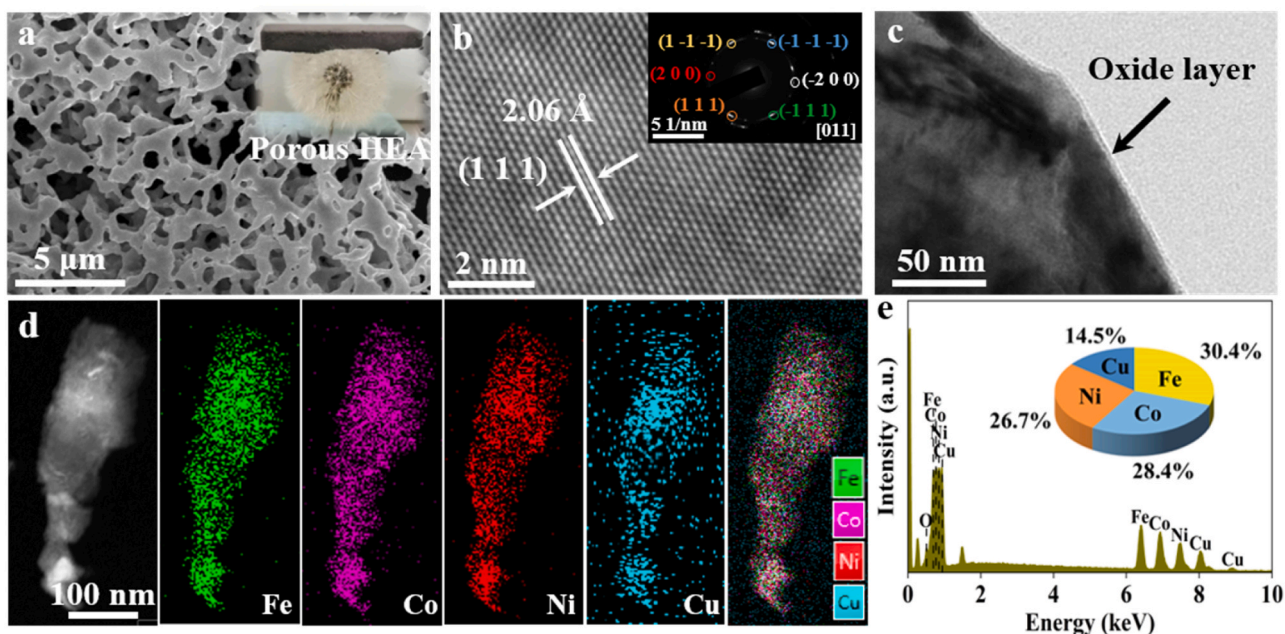
Fig. 4. (a) SEM images of porous FeCoNiCu$_{0.5}$ HEA, (b) HAADF-STEM images with corresponding FFT images at the selected positions, and (c) HRTEM images of the edge region. (d) HRTEM magnified selected region of porous FeCoNiCu$_{0.5}$ HEA with corresponding elemental distribution map, and (e) EDS spectrum images.

of $-NO_3^-$ near 1050 cm^{-1}[53], the swinging peak of $-CH_2$ near 1316 cm^{-1}[53], the antisymmetric stretching peak of $-C=O$ near 1474 cm^{-1} [53], and the stretching vibration peaks of $-C=O$ coordinated with metal ions as well as $-CH_2$ near 1610 cm^{-1} are all from the dissolved metal nitrates and glycine[53]. While the Raman spectrum of product obtained after solution combustion reaction only retains a broad peak near 500 cm^{-1}, implying the destruction of the complex structures between glycine and metal ions and the formation of composite oxides.

According to the above facts and the property of glycine, it can be inferred that the amino groups in glycine can form coordination bonds with transition metal ions such as Fe^{3+}, Co^{2+}, Ni^{2+}, and Cu^{2+}, while carboxyl groups of glycine also can bind with them ionically. Furthermore, a central metal ion can form multiple ring complexes with several glycine molecules. During the concentration process, the solution gradually increases in the viscosity and finally form gels since the metal ions and glycine molecules form complicated cross-linked network structure containing a large number of protonated water molecules and adsorbed water. As glycine burns, glycine gradually decomposes to produce N_2 and CO_2, while NO_3^- decomposes to produce NO_2. A sharp rise in temperature also causes large amounts of water to evaporate and produce steam. Thus, the gel gradually transforms into the composite oxide precursor.

The infrared spectra of the solution-combustion products before and after calcination are shown in Fig. 2(c). The product before calcination presents the prominent absorption peaks at 3470 cm^{-1}, 1650 cm^{-1}, and 1380 cm^{-1}, representing $-O-H$, $-C=O$, and $-NO_3^-$, respectively. This indicates a handful of glycine and nitrate are retained in the combustion-synthesized powders. These absorption peaks of the sample after being annealed at 400 °C is weakened or disappeared, indicating a higher purity of the composite oxide precursor. XRD analysis also shows that the composite oxide precursor is composed of multiple oxides such as Fe_3O_4 (JCPDS No. 96–900–2327), Co_3O_4 (JCPDS No. 01–078–1969), NiO (JCPDS No. 01–089–3080), and CuO (JCPDS No. 01–089–5898), as shown in Fig. 2(d).

The glycine combustion synthesis method exhibits self-propagating combustion characteristics. Once the gel reaches its ignition point, the combustion starts and rapidly propagates until all the gel is completely burned, yielding fluffy powders. The ratio of metal nitrates to glycine significantly affects the gel structure and the self-propagating

combustion regime[54], thereby influencing the morphology of the oxide precursor. Fig. 3(a-c) showcase the morphology of the oxide precursors synthesized at mass ratios of metal nitrates to glycine of 10:1, 8:1, and 6:1, respectively. When the mass ratio is 10:1, the self-propagating combustion of glycine exhibits a non-steady state due to the adequate complex of glycine with the metal ions, resulting in less pronounced expansion effects and a precursor powder with low porosity (Fig. 3a). At 8:1, the self-propagating combustion of the gel exhibits a steady state, yielding a precursor with rich porous structures (Fig. 3b). However, when the mass ratio rises to 6:1, the self-propagating combustion of glycine changes into a thermal explosion state. The large volume of gases generated during combustion cause the gel to shatter due to the intense expansion (Fig. 3c). In Fig. 3(d), the FeCoNiCu$_{0.5}$ precursor prepared with a mass ratio of 8:1 exhibits a well porous structure. The EDS mapping results demonstrate the uniform distribution of all elements, with a Fe/Co/Ni/Cu ratio of 29.8/28.3/27.6/14.3, similar with the atomic ratio of Fe/Co/Ni/Cu in HEAs is examined to be 28.1/27.2/28.4/16.3 by ICP-AES, which is in close agreement with the set ratio (Fig. S2).

Fig. 3(e) shows the BET pore structure distribution of the oxide precursor samples. It is seen that the precursor sample obtained via non-steady combustion exhibits low pore volume and small pore sizes. The most prominent pore size is approximately 10 nm. Under steady combustion state, the pore size distribution of the precursor follows a normal distribution spanning the entire mesoporous range (2–50 nm). The most frequent pore size is approximately 20 nm. This indicates that under steady combustion state, the development of voids is more sufficient, and the tension and gas release of the colloid reach a better balance. In fact, as shown in Fig. 3(d), the obtained precursor also contains a large number of micron-sized pores, which are beyond the range of BET testing. However, an excessive amount of glycine addition leads to rapid heat release during the thermal burst reaction. As indicated by the pore size distribution results, micro-pores are the main pore type in this case, with fewer mesoporous pores compared to the steady combustion conditions. Fig. 3(f) shows that the adsorption-desorption curves of the three samples all exhibit hysteresis loops, but without a distinct saturation adsorption plateau, indicating the non-uniformity of the pore structure. According to the BET method, the specific surface area of the oxide precursor obtained via steady combustion is as high as
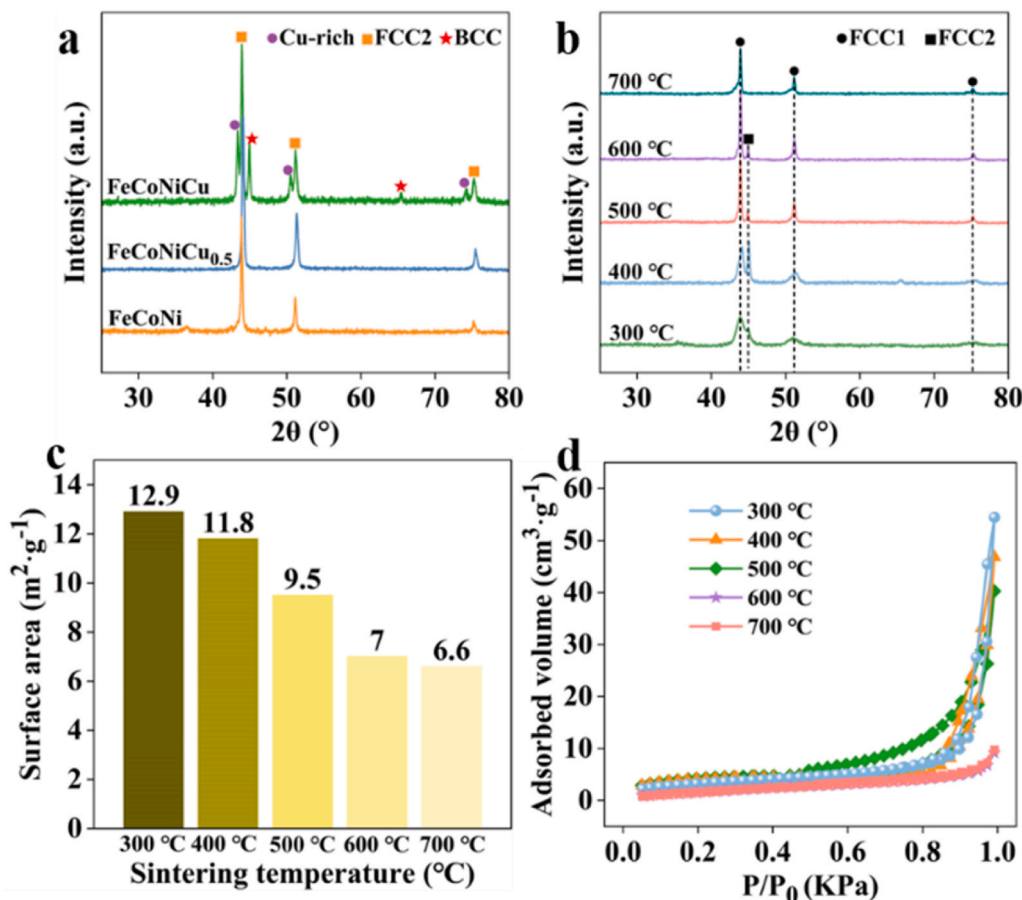
Fig. 5. (a) XRD patterns of FeCoNiCu$_x$ (x=0, 0.5, 1.0) after reduction at 700 °C. (b) XRD patterns, (c) BET specific surface area, and (d) adsorption-desorption isotherms of porous FeCoNiCu$_{0.5}$ HEAs after reduction at 300–700 °C.

39.1 m$^2 \cdot$g^{-1}, while the other two samples are much lower. The higher specific surface area would certainly contribute to the better performance of HEAs electrocatalyst. Therefore, the oxide precursors synthesized at steady combustion were used for the preparation of HEAs.

The loose-fitted precursor powders packed in refractory vessel with dimensions of 4.12 cm in length, 1.45 cm in width, and 0.75 cm in height were heated in hydrogen atmosphere. The microstructure of the reduced product with predetermined FeCoNiCu$_{0.5}$ composition are shown in Fig. 4(a). It is seen that the abundant porosity of the oxide precursor is maintained after H$_2$ reduction. The reduced product has a density of only 56.3 mg$\cdot$cm^{-3}, and it can even be placed on a dandelion flower. HRTEM image indicates the crystallinity of prepared porous FeCoNiCu$_{0.5}$ HEA, see Fig. 4(b). The well-resolved lattice fringes with a spacing of 2.06 Å corresponds to the (111) plane of the FeCoNiCu$_{0.5}$ alloy. Fast Fourier transform (FFT) analysis of the corresponding region displays diffraction patterns in the [011] zone axis, indicating thorough reduction of the precursor (Fig. 4b). Moreover, a thin oxide layer with a thickness of only a few nanometers was observed on the surface of the FeCoNiCu$_{0.5}$ alloy (Fig. 4c). This thin layer is likely to be formed due to the inevitable oxidation when exposed to air. TEM-EDS analysis confirms the homogeneous distribution of all elements in the FeCoNiCu$_{0.5}$ alloy (Fig. 4d). The ratios of Fe/Co/Ni/Cu were found to be 30.4/28.4/26.7/14.5 at%, respectively, which closely matches the proportion of the precursor powders (Fig. 4e).

Composition segregation caused by immiscible elements can affect the mixing entropy of FeCoNiCu alloy. According to the alloy phase diagrams, Cu has limited solid solubility in Ni, and lower solid solubility in Fe and Co. To obtain a single-phase solid solution, it is necessary to control the Cu content. Fig. 5(a) shows the XRD patterns of FeCoNiCu$_x$

alloys with different Cu contents prepared at 700 °C. It is seen that both of the FeCoNi and FeCoNiCu$_{0.5}$ alloy present single FCC phase, while FeCoNiCu$_{1.0}$ alloy shows a three-phase structure. Fig. S3(a-c) display the corresponding SEM images and element distribution mappings of FeCoNi, FeCoNiCu$_{0.5}$, and FeCoNiCu$_{1.0}$ alloy, respectively, revealing that the reduced samples inherit the porous morphology of the precursors. The element distributions of FeCoNi and FeCoNiCu$_{0.5}$ alloy are uniform, while that of FeCoNiCu$_{1.0}$ alloy shows segregation of Cu element. This result concurs with the report that a dual FCC phase structure would be formed in (FeCoNi)$_{1-y}$(Cu$_m$Al)$_y$ when y>0.5[43]. Hence, the FeCoNiCu$_{0.5}$ alloy with a single-phase solid solution was chosen as the research object. In addition to the above-mentioned quaternary alloys, this study also prepared unary, binary, and ternary alloy samples for comparation study, including Ni, FeNi, CoCu, FeCoNi, and FeNiCu, using glycine combustion and hydrogen reduction. The corresponding XRD patterns are shown in Fig. S4, among which except for the CoCu alloy that show the Cu segregation, the remaining samples are single-phase solid solution with rich porosity, and the element distributions are relatively uniform (Fig. S5-S9).

In addition to the impact of composition, the reduction temperature is another key factor affecting the preparation of single-phase high-entropy alloys. The appropriate temperature can enable all elements to reach thermodynamic equilibrium of diffusion and maintain the uniform distribution of elements. Fig. 5(b) shows the XRD patterns of the FeCoNiCu$_{0.5}$ oxide precursor after hydrogen reduction at different temperature. When the reduction temperature is 300 °C, most of the oxides have been reduced. However, the broadening of the diffraction peaks indicates that a solid solution has not been fully formed. At 400–600 °C, the reduced alloy samples exhibit a dual-phase structure
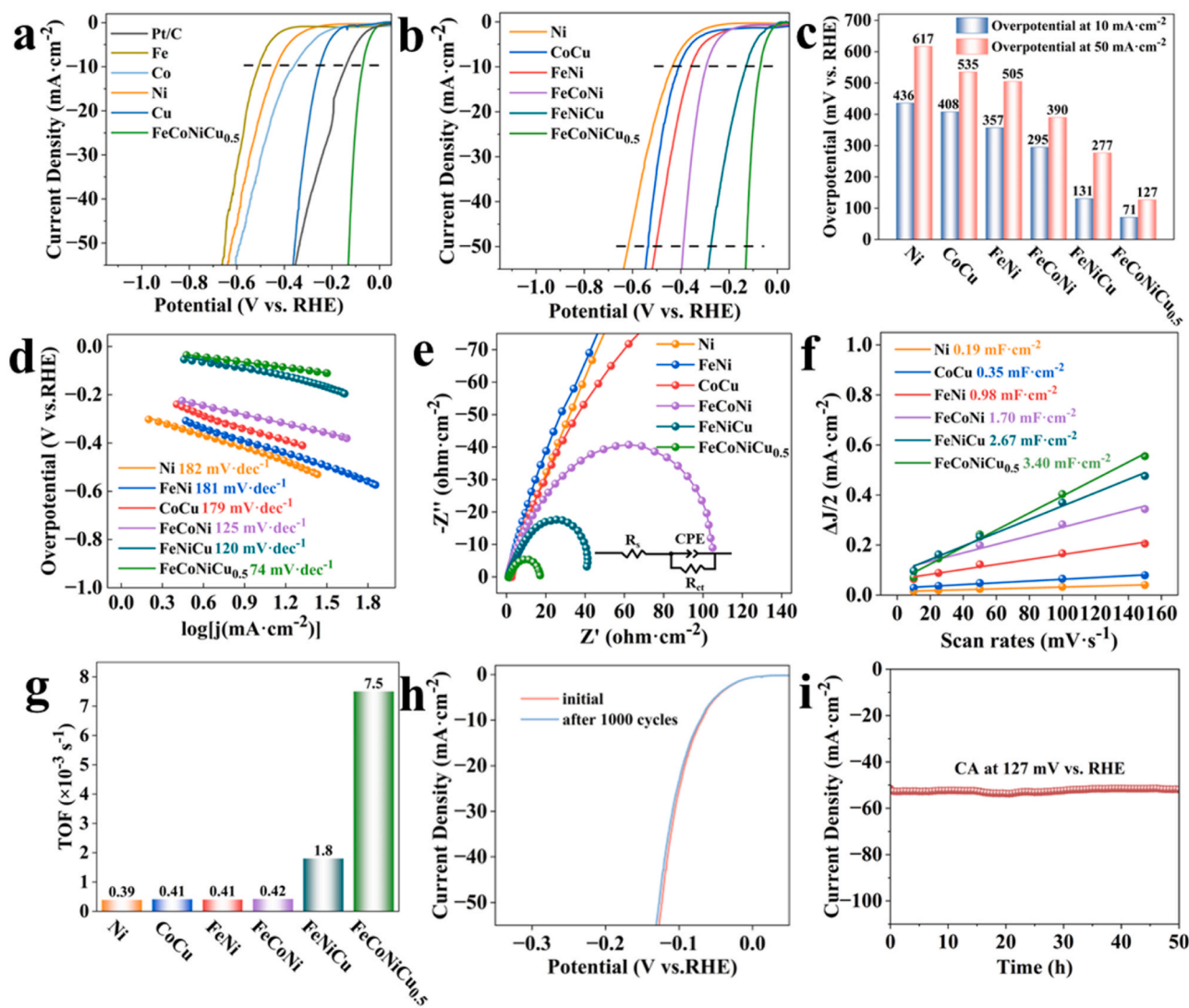
Fig. 6. (a) HER polarization curves of FeCoNiCu$_{0.5}$ and unitary metal catalysts (commercial Pt/C, Fe, Co, Ni, Cu). (b) HER polarization curves, (c) Tafel curves, (d) partial Tafel plots with associated linear fitting results, (e) Nyquist plots, (f) C$_{dl}$ values and (g) TOF values at a current density of 100 mV of FeCoNiCu$_{0.5}$ and unitary (Ni), binary (FeNi, CoCu), and ternary (FeCoNi, FeNiCu) catalysts. (h) HER polarization curves of porous FeCoNiCu$_{0.5}$ HEA before and after 1000 cycle CV test. (i) Long-term stability test of porous FeCoNiCu$_{0.5}$ HEA at 127 mV vs. RHE.

Table 1
EIS fitting parameters of the corresponding parameters achieved from the equivalent circuit for different samples.

Catalysts	R$_s$ (ohm)	R$_{CT}$ (ohm)	CPE-T (a.u.)	CPE-P (a.u.)
Ni	2.49	650.12	0.00030	0.82
FeNi	1.65	523.61	0.00033	0.82
CoCu	2.07	287.85	0.00053	0.82
FeCoNi	1.00	113.10	0.00043	0.77
FeNiCu	1.02	51.60	0.0012	0.79
FeCoNiCu$_{0.5}$	1.12	16.91	0.0067	0.80

with segregation of Cu[43,55]. Increasing the reduction temperature to 700 °C contributes to the solid solution of Cu, forming a single-phase solid solution. Moreover, the specific surface area of the precursor sample decrease from 39.1 m^2·g^{-1} to 6.6 m^2·g^{-1} after hydrogen reduction (Fig. 5c). Note that such specific surface area is still much higher than the common sintered materials[56,57]. As the reduction temperature increases, the number of pores in the sample gradually decrease, and the porous skeleton become densified (Fig. S10). This is manifested by the change of hysteresis loop observed in the BET

adsorption-desorption curves of the samples. The hysteresis loop disappears in the sample after reduction at 600 °C and 700 °C (Fig. 5d). To obtain the porous HEAs with single-phase solid solution and relatively sound mechanical performance. Furthermore, the FeCoNiCu$_{0.5}$ alloy exhibits superior HER performance (Fig. S11). Therefore, this study mainly selected the FeCoNiCu$_{0.5}$ HEAs reduced at 700 °C for the following electrochemical research.

3.2. Hydrogen evolution performance of porous FeCoNiCu$_{0.5}$ HEA

The electrocatalytic HER activity of porous FeCoNiCu$_{0.5}$ was evaluated in a 1 M KOH solution at 25 ℃. To evaluate the synergistic effect between the multiple elements on the HER activity of the porous HEAs, a comparison study was made between FeCoNiCu$_{0.5}$ and unitary, binary, and ternary alloy samples prepared under the same conditions. Fig. 6(a) shows the polarization curves of porous FeCoNiCu$_{0.5}$ and unitary samples at a scanning rate of 10 mV·s^{-1}. It can be observed that the overpotential of porous FeCoNiCu$_{0.5}$ at 10 mA·cm^{-2} is only 71 mV, significantly lower than those of Fe (509 mV), Co (361 mV), Ni (436 mV), Cu (252 mV) and commercial Pt/C (137 mV). Furthermore, the overpotentials of FeCoNiCu$_{0.5}$ at 10 mA·cm^{-2} and 50 mA·cm^{-2} are
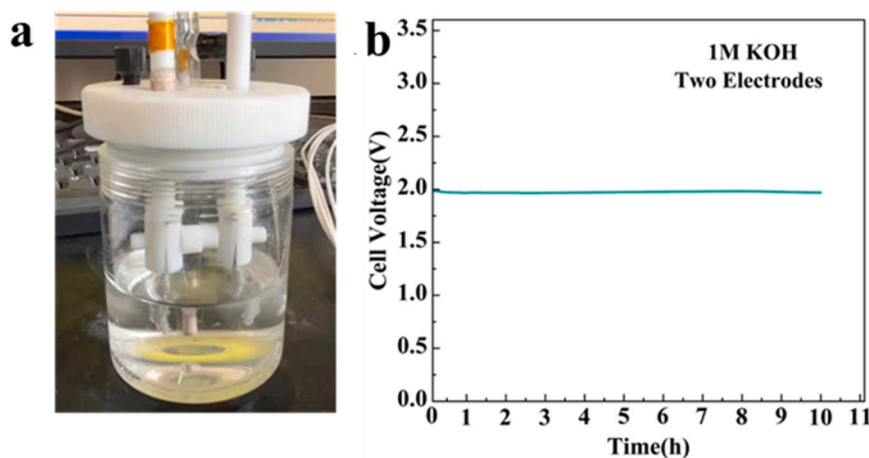
Fig. 7. (a) Image of overall water electrolysis with porous FeCoNiCu$_{0.5}$ HEA as dual electrodes. (b) Chronopotential curve of overall water electrolysis at 10 mA·cm^{-2}.
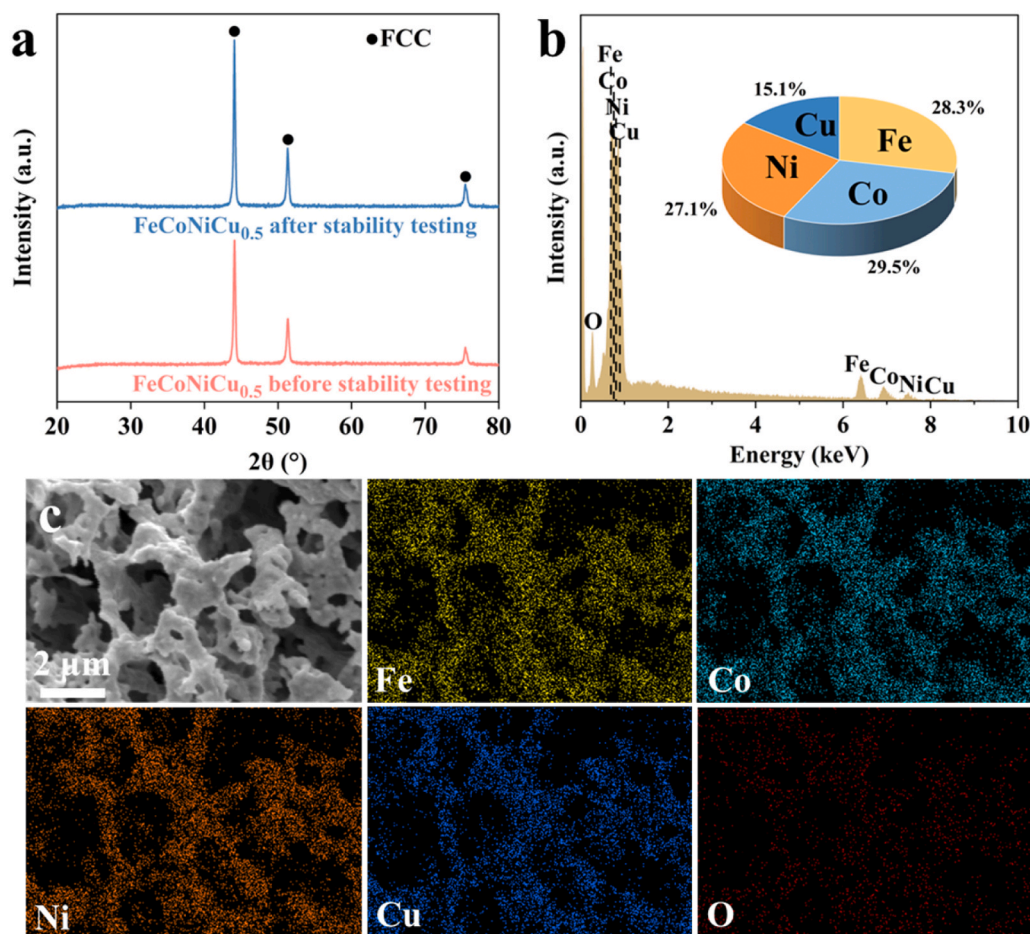
Fig. 8. (a) XRD spectra, (b)EDS spectrum images and (c) SEM image of porous FeCoNiCu$_{0.5}$ HEA before and after stability testing.

also significantly lower than those of other binary and ternary alloys (Fig. 6(b, c)), demonstrating an increased catalytic activity with the increase of alloying elements. The HER activity of porous FeCoNiCu$_{0.5}$ HEA is superior to those of previously reported precious metal, transition metal, oxide, and phosphide catalysts (Table S1). The Tafel slopes obtained from the LSV curves are shown in Fig. 6(d). The Tafel slope of porous FeCoNiCu$_{0.5}$ is 74 mV·dec^{-1}, also superior to other samples. This indicates the fast hydrogen evolution kinetics of porous FeCoNiCu$_{0.5}$ and

that its hydrogen evolution reaction is controlled by the Volmer-Heyrovsky mechanism[56,57]. Fig. S12 illustrate the OER performance of porous FeCoNiCu$_{0.5}$ as anode. It is seen that the polarization curves of porous FeCoNiCu$_{0.5}$ show overpotentials of 377 mV at 10 mA·cm^{-2} and 410 mV at 50 mA·cm^{-2} (Fig. S12a, b), respectively. The Tafel slope is 83.9 mF·cm^{-2} (Fig. S12c). This proves that porous FeCoNiCu$_{0.5}$ can also be used as an anode material and has the potential to server as electrocatalysts for the overall water electrolysis.
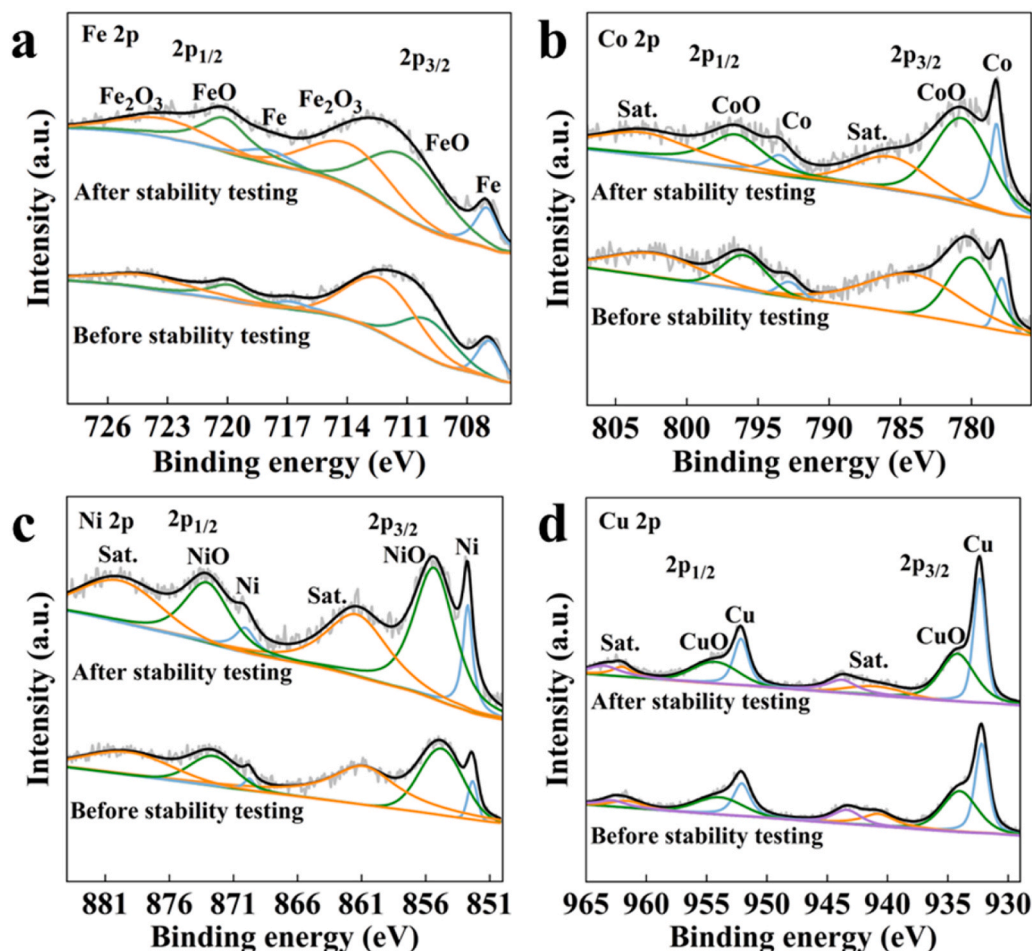
Fig. 9. (a) Fe 2p, (b) Co 2p, (c) Ni 2p, and (d) Cu 2p high-resolution XPS spectra of FeCoNiCu$_{0.5}$ HEA before and after stability testing.

The Nyquist plots of various catalysts all exhibit distinct semicircular curves (Fig. 6(e) and Fig. S13). The arc radius reflects the charge transfer resistance (R$_{ct}$) at the electrode interface. Smaller radius suggests lower resistance to charge transfer. Equivalent circuits of the impedance of each sample were constructed using Zview software, and the Nyquist plots were fitted accordingly with the equivalent circuit to obtain the fitting parameters (Table 1). It is seen that porous FeCoNiCu$_{0.5}$ alloy electrode exhibits the smallest R$_s$ and R$_{CT}$, indicating the highest charge transfer efficiency at the electrode and electrolyte interface. The electrochemical active surface areas (ECSAs) can be evaluated by HEA suring the double-layer capacitance (C$_{dl}$) at non-Faraday area using the CV curves at different sweeping rates (10–150 mV^{-1}), with a testing potential of stable open circuit potential ±0.05 V. The scan curves are shown in Fig. S14 (a-e). It is seen that the porous FeCoNiCu$_{0.5}$ has the highest C$_{dl}$ value (3.40 mF·cm^{-2}) in 1 M KOH (Fig. 6f), indicating the largest electrochemical active surface area (85 m^2·g$_{cat}^{-1}$) (Fig. S15). Fig. S16 normalize ECSAs as the basis for evaluating HER activity. FeCoNiCu$_{0.5}$ HEA still exhibits lower overpotential at 10 mA·cm^{-2} and 50 mA·cm^{-2}, indicating FeCoNiCu$_{0.5}$ HEA has superior electrochemical intrinsic activity. TOF reveals the reaction rate on a single active site and expresses the intrinsic activity of the catalyst. Fig. 6(g) shows the TOF values of the samples at a current density of 100 mV. It can be observed that the TOF value increases with an increase in the number of element components. The TOF value of porous FeCoNiCu$_{0.5}$ is as high as 7.5×10^{-3}·s^{-1}, much higher than other samples. This indicates that the intrinsic activity of the adsorption sites on porous FeCoNiCu$_{0.5}$ HEA also increases.

Fig. 6(h) displays the near-overlapping polarization curves of porous FeCoNiCu$_{0.5}$ HEA before and after 1000 CV cycle tests. Moreover, the

chronopotentiometry method was further used to evaluate the stability of porous FeCoNiCu$_{0.5}$ HEA (Fig. 6i). Due to the influence of the double-layer capacitance, a slight decrease in current density is observed during the initial stage of stability test, a phenomenon commonly observed in HER stability tests. The stable current densities at input voltages of 127 mV vs. RHE coincide with the corresponding current densities shown in Fig. 6(a), and the decrease in current density after 50 h of continuous electrolysis did not exceed 5 %. HEAnwhile, porous FeCoNiCu$_{0.5}$ HEA also shows the stable bath voltage of 1.95 V for overall water electrolysis at 10 mA·cm^{-2} for 10 h (Fig. 7). This indicates the excellent durability of porous FeCoNiCu$_{0.5}$ HEA under alkaline conditions.

Further evidence for the electrode stability was obtained by analyzing the phase composition, morphology, and surface chemical state of porous FeCoNiCu$_{0.5}$ after test. As shown in Fig. 8(a), the XRD pattern of the sample remains almost unchanged after continuous electrolysis for 10 h as compared to the synthesized sample. As shown in Fig. 8(b), the morphology of the samples did not undergo significant changes, and the

elemental ratio of Fe:Co:Ni:Cu is 28.3:29.5:27.1:15.1, comparable to the sample before test (29.8:28.3:27.6:14.3). The morphology of the tested sample also exhibits no significant change (Fig. 8c), indicating good structural stability of porous FeCoNiCu$_{0.5}$ in alkaline conditions.

Chemical states of porous FeCoNiCu$_{0.5}$ before and after stability testing were investigated by XPS. Fig. 9(a) corresponds to Fe 2p spectra which can be divided into subpeaks at 706.8 eV for metal Fe 2p$_{3/2}$, 709.9 eV for FeO 2p$_{3/2}$, 712.3 eV for metal Fe$_2$O$_3$ 2p$_{3/2}$, 716.8 eV for metal Fe 2p$_{1/2}$, 719.9 eV for FeO 2p$_{1/2}$ and 724.0 eV for Fe$_2$O$_3$ 2p$_{1/2}$[13]. In the high-resolution Co 2p spectra displayed in Fig. 9(b), the
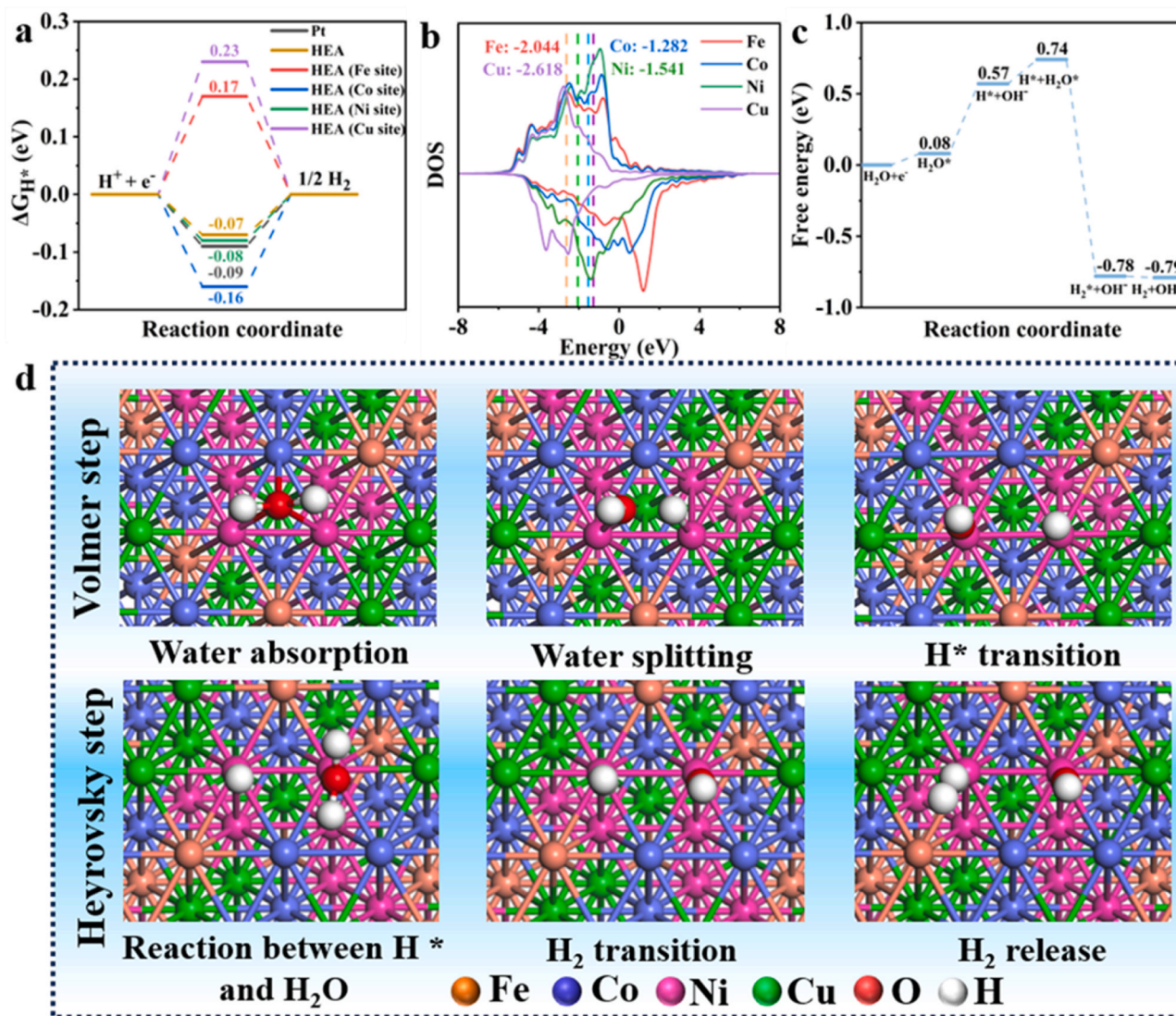
Fig. 10. (a) The ΔG_{H*} of Pt (111), HEA (FeCoNiCu$_{0.5}$), and the Fe, Co, Ni, and Cu sites on FeCoNiCu$_{0.5}$ HEA. (b) The density of states distribution of HEA. (c) The Gibbs free energy change of the Volmer-Heyrovsky reactions. The adsorption process of the Volmer step (d) and the Heyrovsky step (e).

Table 2
The hydrogen adsorption free energy (ΔG_{H*}) of the individual elemental sites in FeCoNiCu$_{0.5}$ HEA with those of pure Fe, Co, Ni, and Cu.

Sites	H*-Case	ΔG_{H*} (eV)
Fe site	H*-Fe	0.21
	H*-FeCoNiCu$_{0.5}$	0.17
Co site	H*-Co	-0.18
	H*-FeCoNiCu$_{0.5}$	-0.16
Ni site	H*-Ni	-0.13
	H*-FeCoNiCu$_{0.5}$	-0.08
Cu site	H*-Cu	0.28
	H*-FeCoNiCu$_{0.5}$	0.23
FeCoNiCu$_{0.5}$	H*-(FeCoNiCu$_{0.5}$)	-0.07
Metal Pt	H*-Pt	-0.09

peaks at binding energies of approximately 778.3 eV and 780.8 eV are consistent with the reported Co 2p$_{3/2}$ values for metal Co and CoO, respectively, whereas the peaks at approximately 793.6 eV and 796.7 eV are also assigned to these two bonds in the Co 2p1/2 region, respectively[13]. In Fig. 9(c), the Ni 2p spectra show the orbitals of metal Ni located at 852.4 eV for 2p$_{3/2}$ and 896.8 eV for 2p$_{1/2}$, as well as peaks at 854.9 eV and 872.8 eV corresponding to NiO 2p$_{3/2}$ and 2p$_{1/2}$,

respectively[58]. The Cu 2p spectra show peaks at 932.3 eV, 934.1 eV, 952.2 eV, and 954.2 eV, which are respectively attributed to Cu 2p$_{3/2}$, CuO 2p$_{3/2}$, Cu 2p$_{1/2}$, and CuO 2p$_{1/2}$[13] (Fig. 9d). These results indicate the presence of metal oxides on the surface of FeCoNiCu$_{0.5}$ electrocatalyst, which is in accord with the thin oxide layer shown in Fig. 3(c). A comparison of the XPS spectra before and after stability tests clearly reveal an increase in the portion of metallic components, which may be due to the reduction of surface oxides during the HER process. In conclusion, porous FeCoNiCu$_{0.5}$ exhibits excellent chemical stability in alkaline electrolytic water.

3.3. First-principles calculation

As shown in Fig. 6, the HER activity of the porous FeCoNiCu$_{0.5}$ HEA is much superior to the related unitary, binary, and ternary alloy samples prepared under the same conditions. To reveal the synergistic effect of different elements in porous FeCoNiCu$_{0.5}$ alloy, the hydrogen adsorption Gibbs free energy (ΔG_{H*}) for FeCoNiCu$_{0.5}$ alloy, various atomic sites in FeCoNiCu$_{0.5}$, and the pure metals (Fe, Co, Ni, Cu) were calculated using density functional theory (DFT). The created crystal models are illustrated in Fig. S17. Pt was chosen as a benchmark catalyst for comparison[59]. It is well known that efficient hydrogen evolution

materials should have appropriate hydrogen adsorption and desorption abilities. The ΔG_{H*} values should be as close to zero as possible. Fig. 10 (a) reveals the ΔG_{H*} values of Fe, Ni, Co and Cu sites in FeCoNiCu$_{0.5}$ alloy, among which Fe, Co, and Cu sites exhibit relatively low hydrogen evolution efficiencies, while Ni site has a ΔG_{H*} value of -0.08 eV, close to that of Pt catalyst (-0.09 eV). In addition, Table 2 demonstrates that the atomic adsorption sites in FeCoNiCu$_{0.5}$ alloy possess lower ΔG_{H*} compared to those in pure metal. According to the volcano plot, these four elements originally do not belong to efficient HER catalysts[17]. but the combination of them as HEA optimizes the electronic structure of each non-noble metal element, thereby enhancing the catalytic activity of the adsorption sites. The ΔG_{H*} value of FeCoNiCu$_{0.5}$ is only -0.07 eV, which is better than Pt. Hence, this indicates the synergistic effect of the different elements in FeCoNiCu$_{0.5}$ alloy facilitates the efficiency for H* adsorption and H$_2$ desorption.

Fig. 10(b) shows the density of states (DOS) distribution of FeCoNiCu$_{0.5}$ high-entropy alloy (HEA). It is worth noting that there is significant overlap between the d orbitals of different elements, indicating strong interactions between the energy bands of different metal components[24]. Furthermore, previous studies have suggested that the optimal adsorption site for H* is around -1.3 eV[58], with the Co 3d orbital at -1.282 eV and the Ni 3d orbital at -1.541 eV. This indicates that both the Co site and the Ni site possess suitable adsorption and desorption capabilities for H*, resulting in lower ΔG_{H*} values. Additionally, the similar positions of the upper half of the Co and Ni orbitals may further facilitate electron transfer. The overlap of the d orbitals not only enhances electron transfer but also exerts a pinning effect on the d orbitals of the Co and Ni sites, thus improving the electrocatalytic activity. On the other hand, the distribution range of the Fe 3d and Cu 3d orbitals spans from -4.0–4.0 eV, enabling flexible electronic modulation and accelerating the transfer of near-surface electrons in the HEA[6, 60]. Considering that the hydrogen evolution rate of FeCoNiCu$_{0.5}$ HEA is predominantly influenced by the Heyrovsky step, the energy consumption of the Volmer-Heyrovsky process (Fig. 10(c)) and the adsorption process (Fig. 10(d, e)) were calculated under alkaline conditions. These include three steps: (i) the physical adsorption of water molecules on the Co and Ni sites, followed by their decomposition into H* and OH$^-$, with H* adsorbed on the Ni site; (ii) another water molecule adsorbing on the Ni site, reacting with H* to form H$_2$* and OH$^-$; (iii) the desorption of H$_2$* and OH$^-$ from the catalyst surface, completing the cycle of alkaline HER. The aforementioned theoretical calculations demonstrate that FeCoNiCu$_{0.5}$ HEA can achieve HER promotion through the synergistic effects of its constituent elements.

4. Conclusions

This study reported the successful synthesis of porous FeCoNiCu high-entropy alloys using glycine solution combustion and hydrogen reduction method. During the solution process, the metal ions of nitrates chelate with glycine and the solution was concentrated until tansforming into gel. The self-propagating combustion initiated by glycine resulted in the porous oxide precursor. When the mass ratio of metal nitrates to glycine was 8:1, the steady combustion took place, which contributed to porous morphology and high specific surface area of composite oxide precursor. The oxide precursor with FeCoNiCu$_{0.5}$ molar ratio was reduced under hydrogen atmosphere at optimal temperature of 700 °C. The prepared porous FeCoNiCu$_{0.5}$ HEA showed over potentials of 71 mV and 127 mV at 10 mA·cm^{-2} and 50 mA·cm^{-2}, respectively, surpassing other unitary, binary, and ternary alloy samples. The porous FeCoNiCu$_{0.5}$ HEA also presented excellent electrochemical stability during alkaline HER after 1000 CV cycles or 50 h of continuous electrolysis. In-depth understanding via various characterizations and DFT calculations shows the electronic interaction between Fe, Co, Ni and Cu elements, and their synergistic effect in modulating the H* adsorption energy and enhancing the HER catalytic activity. This work provides the way for the design of efficient HER high-entropy alloy

catalysts based on low-cost transition metals and unfold the prospect for developing a broad range of advanced materials via glycine solution combustion and hydrogen reduction method.

CRediT authorship contribution statement

Guoqu Zheng: Resources, Investigation. **Huibin Zhang:** Writing – review & editing, Methodology, Funding acquisition, Formal analysis. **Yonghao Zhao:** Resources, Funding acquisition. **Yilin Zhang:** Writing – review & editing, Software, Data curation. **Fei Guo:** Writing – review & editing, Writing – original draft, Methodology, Data curation. **Leilei Wan:** Software, Resources. **Botao Shen:** Writing – review & editing, Data curation. **Huazhen Cao:** Methodology, Investigation. **Guangya Hou:** Supervision, Resources.

Declaration of Competing Interest

Data Availability

Data will be made available on request.

Acknowledgements

Appendix A. Supporting information

Supplementary data associated with this article can be found in the online version at doi:10.1016/j.jallcom.2024.175356.

References

[1] Z.W. Seh, J. Kibsgaard, C.F. Dickens, I. Chorkendorff, J.K. Norskov, T.F. Jaramillo, Combining theory and experiment in electrocatalysis: Insights into materials design, Science 355 (2017) 6321, https://doi.org/10.1126/science.aad4998.

[2] L.Y. Zhang, T. Zeng, L. Zheng, Y. Wang, W. Yuan, M. Niu, C.X. Guo, D. Cao, C.M. Li, Epitaxial growth of Pt–Pd bimetallic heterostructures for the oxygen reduction reaction, Adv. Powder Mater. 2 (2023) 100131, https://doi.org/10.1016/j.apmate.2023.100131.

[3] X. Hu, Y. Li, X. Wei, L. Wang, H. She, J. Huang, Q. Wang, Preparation of double-layered Co−Ci/NiFeOOH co-catalyst for highly meliorated PEC performance in water splitting, Adv. Powder Mater. 1 (2022) 100024, https://doi.org/10.1016/j.apmate.2021.11.010.

[4] H.A. Gasteiger, N.M. Markovic, Chemistry. Just a dream–or future reality? Science 324 (2009) 48–49, https://doi.org/10.1126/science.1172083.

[5] N. Armaroli, V. Balzani, The future of energy supply: Challenges and opportunities, Angew. Chem. Int. Ed. Engl. 46 (2007) 52–66, https://doi.org/10.1002/anie.200602373.

[6] M. Wei, Y.Y. Sun, F. Ai, S.B. Xi, J.Y. Zhang, J.K. Wang, Stretchable high-entropy alloy nanoflowers enable enhanced alkaline hydrogen evolution catalysis, Appl. Catal., B 334 (2023) 122814, https://doi.org/10.1016/j.apcatb.2023.122814.

[7] M. Xia, Y. zhang, J. Xiao, P. Zhao, Z. Hou, F. Du, D. Chen, S. Dou, Magnetic field induced synthesis of (Ni, Zn)Fe$_2$O$_4$ spinel nanorod for enhanced alkaline hydrogen evolution reaction, Prog. Nat. Sci. Mater. 33 (2023) 172–177, https://doi.org/10.1016/j.pnsc.2023.04.001.

[8] J. Feng, L. Qiao, P. Zhou, H. Bai, C. Liu, C.C. Leong, Y.Y. Chen, W.F. Ip, J. Ni, H. Pan, Nanocrystalline CoOxglass for highly-efficient alkaline hydrogen evolution reaction, J. Mater. Chem. A 11 (2023) 316–329, https://doi.org/10.1039/d2ta08073g.

[9] Z.H. Zang, Y.Y. Ren, X. Li, Y.H. Cheng, L.L. Li, X.F. Yu, X.J. Yang, Z.M. Lu, X.H. Zhang, H. Liu, Interfacial microenviroment regulation of FeOOH/S-Co heterostructure catalysts S atoms for overall water splitting, J. Mater. Chem. A 11 (2023) 24618–24628, https://doi.org/10.1039/d3ta05613a.

[10] H. Zhu, S.H. Sun, J.C. Hao, Z.C. Zhuang, S.G. Zhang, T.D. Wang, Q. Kang, S.L. Lu, X.F. Wang, F.L. Lai, T.X. Liu, G.H. Gao, M.L. Du, D.S. Wang, A high-entropy atomic environment converts inactive to active sites for electrocatalysis, Energy Environ. Sci. 16 (2023) 619–628, https://doi.org/10.1039/d2ee03185j.

[11] G. Feng, F. Ning, J. Song, H. Shang, K. Zhang, Z. Ding, P. Gao, W. Chu, D. Xia, Sub-2 nm Ultrasmall High-Entropy Alloy Nanoparticles for Extremely Superior Electrocatalytic Hydrogen Evolution, J. Am. Chem. Soc. 143 (2021) 17117–17127, https://doi.org/10.1021/jacs.1c07643.

[12] A.K. Ipadeola, A.K. Lebechi, L. Gaolatlhe, A.B. Haruna, M. Chitt, K. Eid, A. M. Abdullah, K. Ozoemena, Porous high-entropy alloys as efficient electrocatalysts for water-splitting reactions, Electrochem. Commun. 136 (2022), https://doi.org/10.1016/j.elecom.2022.107207.

[13] K. Huang, J. Xia, Y. Lu, B. Zhang, W. Shi, X. Cao, X. Zhang, L.M. Woods, C. Han, C. Chen, T. Wang, J. Wu, Y. Huang, Self-Reconstructed Spinel Surface Structure Enabling the Long-Term Stable Hydrogen Evolution Reaction/Oxygen Evolution Reaction Efficiency of FeCoNiRu High-Entropy Alloyed Electrocatalyst, Adv. Sci. 10 (2023) 2300094, https://doi.org/10.1002/advs.202300094.

[14] G. Zhao, W. Ma, X. Wang, Y. Xing, S. Hao, X. Xu, Self-water-absorption-type two-dimensional composite photocatalyst with high-efficiency water absorption and overall water-splitting performance, Adv. Powder Mater. 1 (2022) 100008, https://doi.org/10.1016/j.apmate.2021.09.008.

[15] D. Zhang, Y. Shi, H. Zhao, W.J. Qi, X.L. Chen, T.R. Zhan, S.X. Li, B. Yang, M.Z. Sun, J.P. Lai, B.L. Huang, L. Wang, The facile oil-phase synthesis of a multi-site synergistic high-entropy alloy to promote the alkaline hydrogen evolution reaction, J. Mater. Chem. A 9 (2021) 889–893, https://doi.org/10.1039/d0ta10574k.

[16] H.J. Kim, H.Y. Kim, J. Joo, S.H. Joo, J.S. Lim, J. Lee, H. Huang, M. Shao, J. Hu, J. Y. Kim, B.J. Min, S.W. Lee, M. Kang, K. Lee, S. Choi, Y. Park, Y. Wang, J. Li, Z. Zhang, J. Ma, S.I. Choi, Recent advances in non-precious group metal-based catalysts for water electrolysis and beyond, J. Mater. Chem. A 10 (2022) 50–88, https://doi.org/10.1039/d1ta06548c.

[17] J. Li, S. Wang, J. Chang, L. Feng, A review of Ni based powder catalyst for urea oxidation in assisting water splitting reaction, Adv. Powder Mater. 1 (2022) 100030, https://doi.org/10.1016/j.apmate.2022.01.003.

[18] X. Cui, Y. Liu, Y. Chen, Ultrafast micro/nano-manufacturing of metastable materials for energy, Natl. Sci. Rev. 11 (2024) nwae033, https://doi.org/10.1093/nsr/nwae033.

[19] J.W. Yeh, S.K. Chen, S.J. Lin, J.Y. Gan, T.S. Chin, T.T. Shun, C.H. Tsau, S.Y. Chang, Nanostructured High-Entropy Alloys with Multiple Principal Elements: Novel Alloy Design Concepts and Outcomes, Adv. Eng. Mater. 6 (2004) 299–303, https://doi.org/10.1002/adem.200300567.

[20] Y. Yao, Q. Dong, A. Brozena, J. Luo, J. Miao, M. Chi, C. Wang, I.G. Kevrekidis, Z. J. Ren, J. Greeley, G. Wang, A. Anapolsky, L. Hu, High-entropy nanoparticles: Synthesis-structure-property relationships and data-driven discovery, Science 376 (2022) 6589, https://doi.org/10.1126/science.abn3103.

[21] Y. Yao, Z. Huang, P. Xie, S.D. Lacey, R.J. Jacob, H. Xie, F. Chen, A. Nie, T. Pu, M. Rehwoldt, D. Yu, M.R. Zachariah, C. Wang, R. Shahbazian-Yassar, J. Li, L. Hu, Carbothermal shock synthesis of high-entropy-alloy nanoparticles, Science 359 (2018) 1489–1494, https://doi.org/10.1126/science.aan5412.

[22] J. Zhang, Z. Zhao, Q. Li, J. Luan, C.T. Liu, Y. Zhao, T. Yang, Unveiling the unique bifunctionality of L12-structured nanoprecipitates in a FeCoNiAlTi-type high-entropy alloy, Adv. Powder Mater. 2 (2023) 100113, https://doi.org/10.1016/j.apmate.2023.100113.

[23] S. Im, D. Kim, S. Surendran, J. Choi, D.J. Moon, J.Y. Kim, H. Lee, D.H. Nam, U. Sim, High entropy alloy: From theoretical evaluation to electrocatalytic activity of hydrogen evolution reaction, Curr. Opin. Electro 39 (2023) 101293, https://doi.org/10.1016/j.coelec.2023.101293.

[24] T.A.A. Batchelor, J.K. Pedersen, S.H. Winther, I.E. Castelli, K.W. Jacobsen, J. Rossmeisl, High-Entropy Alloys as a Discovery Platform for Electrocatalysis, Joule 3 (2019) 834–845, https://doi.org/10.1016/j.joule.2018.12.015.

[25] X.B. Fu, J.H. Zhang, S.Q. Zhan, F.J. Xia, C.J. Wang, D.S. Ma, Q. Yue, J.S. Wu, Y. J. Kang, High-Entropy Alloy Nanosheets for Fine-Tuning Hydrogen Evolution, ACS Catal. 12 (2022) 11955–11959, https://doi.org/10.1021/acscatal.2c02778.

[26] Y. Xin, S.H. Li, Y.Y. Qian, W.K. Zhu, H.B. Yuan, P.Y. Jiang, R.H. Guo, L.B. Wang, High-Entropy Alloys as a Platform for Catalysis: Progress, Challenges, and Opportunities, ACS Catal. 10 (2020) 11280–11306, https://doi.org/10.1021/acscatal.0c03617.

[27] A. Sivanantham, H. Lee, S.W. Hwang, B. Ahn, I.S. Cho, Preparation, electrical and electrochemical characterizations of CuCoNiFeMn high-entropy-alloy for overall water splitting at neutral-pH, J. Mater. Chem. A 9 (2021) 16841–16851, https://doi.org/10.1039/d1ta02621f.

[28] L. Fan, Y. Ji, G. Wang, J. Chen, K. Chen, X. Liu, Z. Wen, High Entropy Alloy Electrocatalytic Electrode toward Alkaline Glycerol Valorization Coupling with Acidic Hydrogen Production, J. Am. Chem. Soc. 144 (2022) 7224–7235, https://doi.org/10.1021/jacs.1c13740.

[29] Y. He, X. Zhu, C. Zhang, Z. Liu, B. Cao, L. Sheng, Y. Yang, Q. Feng, N. Wang, J. Z. Ou, Y. Xu, Self-Circulating Adsorption–Desorption Structure of Non-Noble High-Entropy Alloy Electrocatalyst Facilitates Efficient Water Splitting, ACS Sustain. Chem. Eng. 11 (2023) 5055–5064, https://doi.org/10.1021/acssuschemeng.2c06888.

[30] Z. Jia, T. Yang, L. Sun, Y. Zhao, W. Li, J. Luan, F. Lyu, L.C. Zhang, J.J. Kruzic, J. J. Kai, J.C. Huang, J. Lu, C.T. Liu, A Novel Multinary Intermetallic as an Active Electrocatalyst for Hydrogen Evolution, Adv. Mater. 32 (2020) 2000385, https://doi.org/10.1002/adma.202000385.

[31] S. Kasatikov, A. Fantin, A.M. Manzoni, S. Sakhonenkov, A. Makarova, D. Smirnov, E.O. Filatova, G. Schumacher, Chemical interaction and electronic structure in a compositionally complex alloy: A case study by HEAns of X-ray absorption and X-ray photoelectron spectroscopy, J. Alloy. Compd. 857 (2021) 157597, https://doi.org/10.1016/j.jallcom.2020.157597.

[32] G. Cao, J. Liang, Z. Guo, K. Yang, G. Wang, H. Wang, X. Wan, Z. Li, Y. Bai, Y. Zhang, J. Liu, Y. Feng, Z. Zheng, C. Lu, G. He, Z. Xiong, Z. Liu, S. Chen, Y. Guo, M. Zeng, J. Lin, L. Fu, Liquid metal for high-entropy alloy nanoparticles synthesis, Nature 619 (2023) 73–77, https://doi.org/10.1038/s41586-023-06082-9.

[33] F. Waag, Y. Li, A.R. Ziefuss, E. Bertin, M. Kamp, V. Duppel, G. Marzun, L. Kienle, S. Barcikowski, B. Gokce, Kinetically-controlled laser-synthesis of colloidal high-entropy alloy nanoparticles, RSC Adv. 9 (2019) 18547–18558, https://doi.org/10.1039/c9ra03254a.

[34] X. Cui, Y. Liu, X. Wang, X. Tian, Y. Wang, G. Zhang, T. Liu, J. Ding, W. Hu, Y. Chen, Rapid High-Temperature Liquid Shock Synthesis of High-Entropy Alloys for Hydrogen Evolution Reaction, ACS Nano 18 (2024) 2948–2957, https://doi.org/10.1021/acsnano.3c07703.

[35] S. Yuan, X. Zhu, H. Li, Z. Hu, Q. Ren, W. Zhao, X. Tang, S. Hu, Ultrathin wavy nanowires of high-entropy alloy as cocktail solution in methanol oxidation reaction, Prog. Nat. Sci. Mater. 33 (2023) 225–231, https://doi.org/10.1016/j.pnsc.2023.05.006.

[36] C. Qin, W. Wu, H. Gomaa, S. Wu, C. An, Q. Deng, N. Hu, Hydrogel-based catalysts for hydrogen generation by the hydrolysis of B–H compounds under external physical fields, J. Energy Chem. 86 (2023) 518–535, https://doi.org/10.1016/j.jechem.2023.07.027.

[37] D. Wen, A.K. Herrmann, L. Borchardt, F. Simon, W. Liu, S. Kaskel, A. Eychmuller, Controlling the growth of palladium aerogels with high-performance toward bioelectrocatalytic oxidation of glucose, J. Am. Chem. Soc. 136 (2014) 2727–2730, https://doi.org/10.1021/ja412062e.

[38] X. Xu, Q. Zhang, M. Hao, Y. Hu, Z. Lin, L. Peng, T. Wang, X. Ren, C. Wang, Z. Zhao, C. Wan, H. Fei, L. Wang, J. Zhu, H. Sun, W. Chen, T. Du, B. Deng, G.J. Cheng, I. Shakir, C. Dames, T.S. Fisher, X. Zhang, H. Li, Y. Huang, X. Duan, Double-negative-index ceramic aerogels for thermal superinsulation, Science 363 (2019) 723–727, https://doi.org/10.1126/science.aav7304.

[39] Z. Wang, P. Liu, J. Han, C. Cheng, S. Ning, A. Hirata, T. Fujita, M. Chen, Engineering the internal surfaces of three-dimensional nanoporous catalysts by surfactant-modified dealloying, Nat. Commun. 8 (2017) 1066, https://doi.org/10.1038/s41467-017-01085-3.

[40] T. Fujita, P. Guan, K. McKenna, X. Lang, A. Hirata, L. Zhang, T. Tokunaga, S. Arai, Y. Yamamoto, N. Tanaka, Y. Ishikawa, N. Asao, Y. Yamamoto, J. Erlebacher, M. Chen, Atomic origins of the high catalytic activity of nanoporous gold, Nat. Mater. 11 (2012) 775–780, https://doi.org/10.1038/nmat3391.

[41] A. Qayum, M.R. Guo, J. Wei, S. Dong, X.L. Jiao, D.R. Chen, T. Wang, An combustion method for scale-up fabrication of BiVO photoanodes with enhanced long-term photostability for unassisted solar water splitting, J. Mater. Chem. A 8 (2020) 10989–10997, https://doi.org/10.1039/d0ta03557b.

[42] V. Chaudhary, V. Soni, B. Gwalani, R.V. Ramanujan, R. Banerjee, Influence of non-magnetic Cu on enhancing the low temperature magnetic properties and Curie temperature of FeCoNiCrCu(x) high entropy alloys, Scr. Mater. 182 (2020) 99–103, https://doi.org/10.1016/j.scriptamat.2020.02.037.

[43] Q. Yu, W.W. Xu, C. Cui, X.G. Gong, W. Li, L.J. Chen, X.Q. Li, L. Vitos, Unveiling segregation-induced evolution in phase constitution of Cu-containing high-entropy alloys, J. Alloy. Compd. 843 (2020) 156109, https://doi.org/10.1016/j.jallcom.2020.156109.

[44] D. Kim, J. An, S. Surendran, J. Lim, H.Y. Jeong, S. Im, J. Young Kim, K.T. Nam, U. Sim, Synergistic effect of Polydopamine incorporated Copper electrocatalyst by dopamine oxidation for efficient hydrogen production, J. Colloid Interface Sci. 650 (2023) 1406–1414, https://doi.org/10.1016/j.jcis.2023.06.184.

[45] H. Ghadimi Mahanipour, S.M. Masoudpanah, M. Adeli, S.M.H. Hoseini, Regeneration of LiNi$_{0.6}$Co$_{0.2}$Mn$_{0.2}$O$_2$ material from spent lithium-ion batteries by solution combustion synthesis method, J. Energy Storage 79 (2024) 110192, https://doi.org/10.1016/j.est.2023.110192.

[46] F.T. Li, J. Ran, M. Jaroniec, S.Z. Qiao, Solution combustion synthesis of metal oxide nanomaterials for energy storage and conversion, Nanoscale 7 (2015) 17590–17610, https://doi.org/10.1039/c5nr05299h.

[47] A.A. Abdul Salam, S.T. S.M. Kumar, A. Bankapur, R.K. Sinha, L. Simon, S. Chidangil, Effect of OH substitution in 3-benzylchroman-4-ones: crystallographic, CSD, DFT, FTIR, Hirshfeld surface, and energy framework analysis, RSC Adv. 11 (2021) 20123–20136, https://doi.org/10.1039/d1ra02245h.

[48] E. Emil-Kaya, S. Stopic, S. Gurmen, B. Friedrich, Production of rare earth element oxide powders by solution combustion: a new approach for recycling of NdFeB magnets, RSC Adv. 12 (2022) 31478–31488, https://doi.org/10.1039/d2ra05876f.

[49] I. Aswin Kumar, M. Naushad, T. Ahamad, N. Viswanathan, Facile fabrication of tunable porous zirconium fumarate based metal organic frameworks in the retention of nutrients from water, Environ. Sci.: Water Res. Technol. 6 (2020) 2856–2870, https://doi.org/10.1039/D0EW00385A.

[50] J. Al Boukhari, M. Noun, R. Awad, Raman spectroscopic investigations of pure, (Mg, Cu), and (Mg, Ru) codoped NiO nanoparticles, Chem. Phys. Lett. 836 (2024) 141508, https://doi.org/10.1016/j.cplett.2023.141508.

[51] Z. Qiu, Y. Ma, T. Edvinsson, In operando Raman investigation of Fe doping influence on catalytic NiO intermediates for enhanced overall water splitting, Nano Energy 66 (2019) 104118, https://doi.org/10.1016/j.nanoen.2019.104118.

[52] S.O. Jung, R.A. Senthil, C.J. Moon, N. Tarasenka, A.H. Min, S.J. Lee, N. Tarasenko, M.Y. Choi, Mechanistic insights into ZIF-67-derived Ir-doped Co$_3$O$_4$@N-doped carbon hybrids as efficient electrocatalysts for overall water splitting using in situ Raman spectroscopy, Chem. Eng. J. 468 (2023) 143717, https://doi.org/10.1016/j.cej.2023.143717.

[53] A. Parameswari, S. Premkumar, R. Premkumar, A.M.F. Benial, Surface enhanced Raman spectroscopy and quantum chemical studies on glycine single crystal, J. Mol. Struct. 1116 (2016) 180–187, https://doi.org/10.1016/j.molstruc.2016.03.025.

[54] X.L. Wang, M.L. Qin, F. Fang, B.R. Jia, H.Y. Wu, X.H. Qu, A.A. Volinsky, Effect of glycine on one-step solution combustion synthesis of magnetite nanoparticles, J. Alloy. Compd. 719 (2017) 288–295, https://doi.org/10.1016/j.jallcom.2017.05.187.

[55] A.M. Garrett, C.P. Race, Ab-initio calculations of substitutional co-segregation interactions at coherent bcc Fe-Cu interfaces, J. Nucl. Mater. 569 (2022) 153923, https://doi.org/10.1016/j.jnucmat.2022.153923.

[56] H. Zhang, F. Guo, L. Wan, Z. Gao, T. Chen, H. Cao, H. Chen, G. Zheng, Performance assessments of porous FeCoNiCrAl$_x$ high-entropy alloys in high-temperature oxidation, carbonization and sulfidation atmospheres, J. Alloy. Compd. 930 (2023) 167437, https://doi.org/10.1016/j.jallcom.2022.167437.

[57] H.B. Zhang, H.Y. Gao, X.L. Liu, H. Yu, L.F. Wang, Y. Jiang, L. Gao, L.P. Yu, Y.H. He, X.M. Chen, L. Zhang, G.Q. Zheng, Reactive synthesis and assessment of porous Fe-20.5Al-18Cr intermetallic material: A comparative study with porous FeCrAl material produced from prealloyed powders, Sep. Purif. Technol. 220 (2019) 152–161, https://doi.org/10.1016/j.seppur.2019.03.054.

[58] C. Zhan, Y. Xu, L. Bu, H. Zhu, Y. Feng, T. Yang, Y. Zhang, Z. Yang, B. Huang, Q. Shao, X. Huang, Subnanometer high-entropy alloy nanowires enable remarkable hydrogen oxidation catalysis, Nat. Commun. 12 (2021) 6261, https://doi.org/10.1038/s41467-021-26425-2.

[59] D. Kim, S. Surendran, Y. Jeong, Y. Lim, S. Im, S. Park, J.Y. Kim, S. Kim, T.H. Kim, B. Koo, K. Jin, U. Sim, Electrosynthesis of Low Pt-Loaded High Entropy Catalysts for Effective Hydrogen Evolution with Improved Acidic Durability, Adv. Mater. Technol. 8 (2022) 2200882, https://doi.org/10.1002/admt.202200882.

[60] Z. Hu, K. Chen, Y. Zhu, B. Liu, J. Shen, Synergistic Effects of PtRhNiFeCu High Entropy Alloy Nanocatalyst for Hydrogen Evolution and Oxygen Reduction Reactions, Small 20 (2024) 2309819, https://doi.org/10.1002/smll.202309819.